Paper Number: **1102** *(replace with your paper number)*

Title: **Modeling Fatigue Damage Onset and Progression in Composites Using an Element-Based Virtual Crack Closure Technique Combined with the Floating Node Method**

Authors: Nelson V. De Carvalho
Ronald Krueger

(FIRST PAGE OF ARTICLE – *align this to the top of page – leave space blank above ABSTRACT*)

ABSTRACT

A new methodology is proposed to model the onset and propagation of matrix cracks and delaminations in carbon-epoxy composites subject to fatigue loading. An extended interface element, based on the Floating Node Method, is developed to represent delaminations and matrix cracks explicitly in a mesh independent fashion. Crack propagation is determined using an element-based Virtual Crack Closure Technique approach to determine mixed-mode energy release rates, and the Paris-Law relationship to obtain crack growth rate. Crack onset is determined using a stress-based onset criterion coupled with a stress vs. cycle curve and Palmgren-Miner rule to account for fatigue damage accumulation. The approach is implemented in Abaqus/Standard® via the user subroutine functionality. Verification exercises are performed to assess the accuracy and correct implementation of the approach. Finally, it was demonstrated that this approach captured the differences in failure morphology in fatigue for two laminates of identical stiffness, but with layups containing $\theta°$ plies that were either stacked in a single group, or distributed through the laminate thickness.

INTRODUCTION

Fatigue damage in composite materials generally results in a combination of multiple delaminations and matrix cracks. These damage mechanisms are not isolated and often interact, forming complex damage patterns. Few approaches attempt to model these damage modes and their interaction explicitly in fatigue [1,

Nelson V. De Carvalho, R. Krueger, National Institute of Aerospace, 100 Exploration Way, Hampton, VA, 23666. This work was performed at the Durability, Damage Tolerance and Reliability Branch, MS 188E, NASA Langley Research Center, Hampton, VA, 23681, U.S.A.

2]. In [1], both delamination and matrix crack onset are modeled using stress-based criteria and ad-hoc stiffness degradation. Such an approach is mesh-subjective, limiting its applicability as a predictive tool. In [2], both matrix cracks and delamination are modeled with a fatigue cohesive element approach, rendering an approach that can be mesh-objective. Matrix cracks are represented using the regularized Extended Finite Element Method (rXFEM), and delaminations are represented through interface elements. Both damage onset and propagation for matrix cracks and delaminations are modeled through a fatigue cohesive approach [2].

The Floating Node Method (FNM) has been proposed in [3] to represent multiple discontinuities in solids in a mesh independent fashion. The method provides a single approach to model both damage mechanisms (matrix cracks and delamination) and their interaction. Furthermore, one of its main advantages is the simplicity with which multiple cracks and their interaction can be accommodated explicitly within an element.

In the present work, a three-dimensional (3D) extended interface element, based on the FNM, is proposed and combined with an element-based implementation of the Virtual Crack Closure Technique (VCCT) [4] and an onset criterion. The resultant approach is capable of simulating both fatigue damage onset and propagation. In the first section, an overview of the 3D interface element is provided. Subsequently, a description of the element-based VCCT technique and how it is used to propagate both matrix cracks and delaminations is given. Afterwards, the procedure used to determine matrix cracks and delamination onset in fatigue using a stress-based approach while assuming Linear Elastic Fracture Mechanics (LEFM) is described. Two sets of verification exercises for matrix cracks and delaminations are performed to assess accuracy and implementation of the approach being proposed. Finally, the approach is demonstrated by simulating crack onset and accumulation in fatigue in cross-ply laminates with different stacking sequences.

3D CRACK REPRESENTATION IN COMPOSITES USING THE FLOATING NODE METHOD: EXTENDED INTERFACE ELEMENT

In the present work, the FNM [3] was used to develop a 3D extended interface element as shown in Figure 1. This element is used to model an interface and the plies immediately above and below that interface via sub-elements 1 and 2. The plies modeled with sub-elements 1 and 2 can have the same or different orientations and thicknesses. Formulated in this fashion, the extended interface element provides access to the stress state at the interface and within the plies immediately above/below (Figure 1a). Additionally, it enables resolution of the kinematics of multiple crack interaction (delamination/matrix crack) within a single element. Each sub-element can be divided along any vertical plane to represent matrix cracks of any orientation (Figure 1b). In addition to 16 real nodes, the element has a total of 32 floating nodes, which are used as required to represent discontinuities, or are otherwise condensed out of the system of equations. After the initial partitioning, the sub-elements can be further sub-divided as needed for integration purposes. This is illustrated in Figure 1b, sub-element 2, where the green lines represent further subdivisions needed for

integration. No limits to the number of cracks are imposed. Crack spacing is only limited by the assumption that each sub-element can only represent one matrix crack.
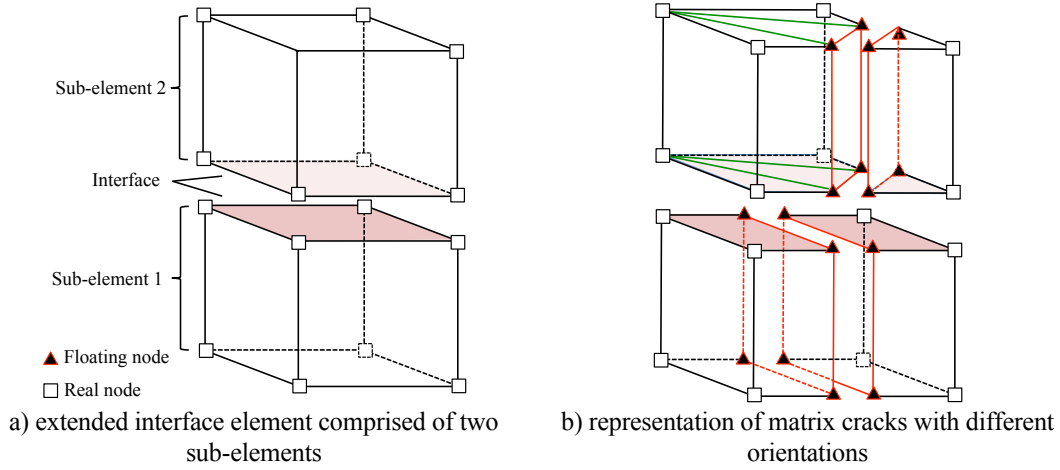

a) extended interface element comprised of two sub-elements

b) representation of matrix cracks with different orientations

Figure 1. Extended interface element with interface and matrix crack representation.

DELAMINATION AND MATRIX CRACK PROPAGATION

Matrix cracks and delaminations are represented with the FNM and the extended interface element summarized above. To determine crack propagation, an element-based VCCT technique is proposed and will be detailed in the next section.

Element-based Virtual Crack Closure Technique (VCCT)

In the element-based VCCT, the shape functions of interface elements are used to obtain tractions and displacements at integration points. The tractions and displacements are then used to compute energy release rates for the elements at the crack front. The same methodology is applied for both matrix cracks and delaminations, as illustrated in Figures 2a and 2b. Figure 2c shows a planar view of a crack front (matrix crack or delamination). For each pair of elements (e_0, e_j), where e_j designates elements adjacent to e_0, energy release rates can be computed in opening mode and shear mode using VCCT as:

$$G_n^{e_0-e_j} = \sum_{i=1}^{I} \frac{\sigma_n^{e_0,i} \delta_n^{e_j,i} A^i}{2A^{e_0}} \tag{1}$$

$$G_s^{e_0-e_j} = \sum_{i=1}^{I} \frac{\tau_s^{e_0,i} \delta_s^{e_j,i} A^i}{2A^{e_0}} \tag{2}$$

$$G_t^{e_0-e_j} = \sum_{i=1}^{I} \frac{\tau_t^{e_0,i} \delta_t^{e_j,i} A^i}{2A^{e_0}} \tag{3}$$

where s and t designate two in-plane orthogonal directions and n is the normal to that plane, as shown in Figure 2c. In equations 1 to 3, A^i corresponds to the area of each integration point i, A^{e_0} to the area of the element e_0, and I is the total number of integration points. The normal traction $\left(\sigma_n^{e_0,i}\right)$, and shear tractions $\left(\tau_s^{e_0,i}, \tau_t^{e_0,i}\right)$ are computed at the integration points of element e_0; and the openings, $\delta_n^{e_j,i}$, $\delta_s^{e_j,i}$, $\delta_t^{e_j,i}$, are obtained at equivalent positions of elements e_j (Figure 2c). The contributions from each integration point pair are summed to obtain the energy releases for each pair of elements. The maximum energy release rate for a pair of elements $\left(e_0, e_j\right)$ is determined as:

$$G_{max}^{e_0-e_j} = G_n^{e_0-e_j} + G_s^{e_0-e_j} + G_t^{e_0-e_j} \tag{4}$$

The maximum energy release for the element e_0, $G_{max}^{e_0}$, is assumed to be the maximum $G_{max}^{e_0-e_j}$ obtained with the four pairs $\left(e_0, e_j\right)$:

$$G_{max}^{e_0} = \max\left\{G_{max}^{e_0-e_1}, \dots, G_{max}^{e_0-e_4}\right\} \tag{5}$$

Once the maximum is determined, the adjacent element e_j^*, associated with the maximum value, is identified. It is then possible to determine the mode-mixity, β^{e_0}, as:

$$\beta^{e_0} = \frac{G_n^{e_0-e_j^*} + G_s^{e_0-e_j^*}}{G_{max}^{e_0}} \tag{6}$$

and the characteristic length, l^{e_0}, corresponding to the length of the common edge between e_0 and e_j^* (see Figure 2 where $e_j^* = e_1$ is assumed). The characteristic length, l^{e_0}, is used in the calculation of the cycles needed for a given element to open, as detailed in the following section.

a) delamination   b) matrix crack
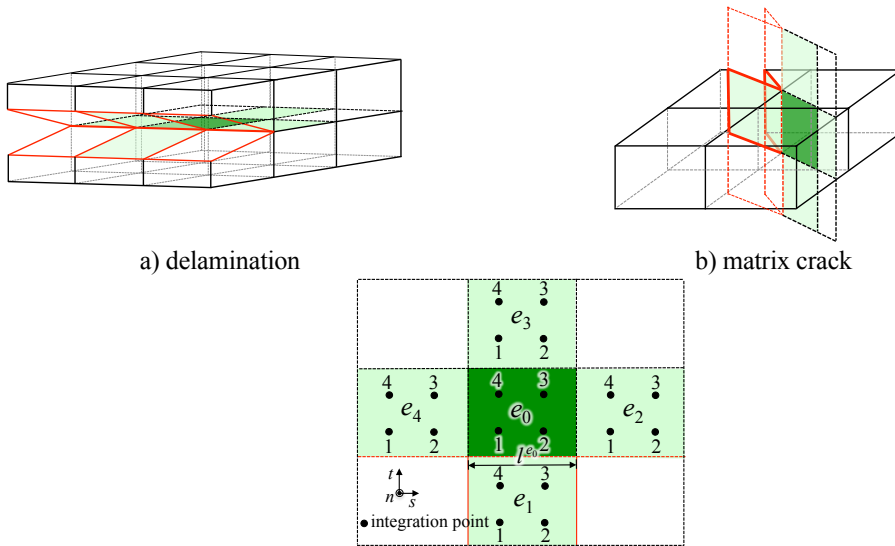
c) crack plane view. The solid circles represent integration points in each element.
Figure 2. Element-based VCCT applied to both delaminations and matrix cracks.

Propagation delamination and matrix cracks

Delaminations and matrix cracks are assumed to propagate following the Paris Law [5] given by:

$$\frac{da}{dN} = c(G_{max})^n \tag{7}$$

where G_{max} corresponds to the maximum energy release rate obtained at peak load, a designates the crack length and N the cycles. The coefficient c and exponent n are assumed to be a piece-wise linear function of the mode-mixity. At a given step s, the energy release rate, mode-mixity, and the growth rate are determined for each element e_k at the crack front. A binary failed/not failed approach is implemented. The un-cracked area $A_{uc}^{e_k}$ is used as an internal state variable that tracks crack accumulation for the elements at the crack front that do not fail in a given step. An element is considered to fail if its un-cracked area $A_{uc}^{e_k}$ is reduced below a fraction f of the original area:

$$A_{uc}^{e_k}\Big|_{s+1} < f A^{e_k} \tag{8}$$

Otherwise the element is considered to be pristine. In the present study, $f = 0.1$, which assumes an element fails if the un-cracked area is less than 10% of the original area. Hence, before damage:

$$A_{uc}^{e_k} = A^{e_k} \tag{9}$$

where A^{e_k} corresponds to the area of the element. The cycles needed to fail each element at the crack front, at step s, can be obtained as:

$$\Delta N^{e_k} = \frac{A_{uc}^{e_k}\Big|_s}{\left(\dfrac{da}{dN}\right)^{e_k} l^{e_k}} \tag{10}$$

in which length l^{e_k} is the characteristic length associated with element e_k. The values of all ΔN^{e_k} are afterwards used to determine the cycle increment in the step, ΔN_{inc}, which is assumed to be the minimum number of cycles needed to fail an element or initiate a new crack. Knowing the cycle increment and the growth rate, the crack increment, ΔA^{e_k}, can be calculated:

$$\Delta A^{e_k} = l^{e_k} \left(\frac{da}{dN}\right)^{e_k} \Delta N_{inc} \tag{11}$$

and an updated un-cracked area obtained as:

$$A_{uc}^{e_k}\Big|_{s+1} = A_{uc}^{e_k}\Big|_s - \Delta A^{e_k} \tag{12}$$

DELAMINATION AND MATRIX CRACK ONSET

In the present work, a stress-based criterion is used to determine fatigue damage onset. The definition of a propagation zone, where the stress criterion is not active, enables the combination of a stress-based criterion for fatigue crack onset with the procedure detailed above for modeling crack growth. The definition of the propagation zone, the onset criterion, and their implementation are discussed in the subsequent sections.

Damage onset

The onset of delaminations and matrix cracks is determined by comparing a maximum principal stress criterion to an assumed stress vs. cycle (S-N) curve and using the Palmgren-Miner rule [6] to account for fatigue damage accumulation not leading to onset.

MAXIMUM PRINCINPAL STRESS CRITERION

For delamination, the maximum (positive) principal stress, σ_1^{del}, is computed in the delamination plane:

$$\sigma_1^{del} = \left(\frac{\sigma_n}{2}\right) + \sqrt{\left(\frac{\sigma_n}{2}\right)^2 + \tau_s^2 + \tau_t^2} \tag{13}$$

in which σ_n, τ_s and τ_t are, respectively, the opening and the two orthogonal shear tractions acting in the delamination plane. Once onset is determined in a given element, the elements immediately adjacent are also considered to have failed, enabling the calculation of energy release rates via VCCT, following the procedure outlined above.

For matrix cracks, the maximum principal stress criterion, is written as:

$$\sigma_1^m = \frac{\sigma_{22}}{2} + \sqrt{\left(\frac{\sigma_{22}}{2}\right) + \sigma_{12}^2 + \sigma_{23}^2} \tag{14}$$

where direction '1' corresponds to the fiber direction, '2' is orthogonal to '1' in-plane and '3' is orthogonal to '1', corresponding to the through-thickness direction. The stress components, σ_{33} and σ_{13}, are assumed to not contribute to the onset of matrix cracks. Their effect is accounted for in the delamination onset criterion. The stress in the fiber direction, σ_{11}, is also assumed not to contribute to the onset of matrix cracks. Once matrix crack onset is detected in a given element, the crack is assumed to propagate through the thickness and to the two adjacent elements along the crack direction. This enables the determination of energy release rates via VCCT, and the application of the propagation methodology outlined previously. Additionally, local delaminations are assumed directly above the failed elements, enabling the initiation of local delaminations triggered by matrix cracks.

STRESS VS. CYCLES (S-N) CURVE AND WEIBULL SCALING

Fatigue crack onset in composites is assumed to be reasonably well approximated by an onset curve with the form [7]:

$$S = S_f(1 - \alpha \log(N)) \tag{15}$$

where S_f is the static strength, and α a parameter determined experimentally. The onset of cracks in fatigue is an intrinsically probabilistic event. To capture its probabilistic nature, the static strength in Equation 15 is assumed to follow a Weibull distribution such that the probability of failure at a given stress $P(\sigma)$ is given by [8]:

$$P(\sigma) = 1 - e^{-\left(\frac{\sigma}{\sigma_c}\right)^m} \tag{16}$$

where σ_c is the material characteristic strength and m is the shape parameter. Both σ_c and m can be determined from experimental data. When perfoming the simulations, the distribution is sampled for each element. This procedure inherently leads to a mesh dependent solution: the finer the mesh, more sampling will be performed, and hence the greater the likelihood of obtaining values at the extremes of the assumed distribution. To balance this effect, Weibull scaling is used [8]. Weibull scaling provides a relationship between the strength of two volumes of the same material, based on the notion that the larger the volume, the more likely it is to have a weak link (weakest link assumption). The S-N data used in the present work were obtained using a 3-Point-Bending (3PB) configuration [9]. Using Weibull scaling, the characteristic strength, σ_{c-3PB}, obtained in [9], can be related to the strength of each element, σ_c^e, in a given discretization. Assuming predominantly tensile loading conditions, this relation is given by [9]:

$$\sigma_c^e = \frac{\sigma_{c-3PB}}{\left[2(m+1)^2 \frac{V^e}{V_{3PB}}\right]^{1/m}} \tag{17}$$

where V^e designates the volume of a given element and V_{3PB} is the volume of the 3PB specimen [9]. However in [9], Weibull scaling alone was not sufficient to account for the differences between the strength obtained using a 3PB and a 4-Point-Bending (4PB) test setup, despite predicting the trend correctly. Thus, further investigation may be needed to assess the accuracy of the procedure outlined above.

PALMGREN-MINER RULE

Fatigue damage accumulation prior to the onset of discrete cracks is obtained by the Palmgren-Miner rule [6]:

$$C|_k = \sum_{s=1}^{k} \frac{\Delta N_{inc}|_s}{N_f|_s} \tag{18}$$

where $N_f|_s$ and $\Delta N_{inc}|_s$ are, respectively, the number of cycles to failure and the number of cycles accumulated at the stress corresponding to the sth step. Equation 18 can also be used to determine the cycles needed to fail an element at a given stress level and step k:

$$\Delta N_{onset}|_k = N_f\big|_k (1.0 - C|_{k-1}) \tag{19}$$

In the current implementation, $\Delta N_{onset}|_k$ is computed for all elements at each step. At the end of each step, the minimum number of cycles to onset and/or to propagate a crack is determined and assumed to equal the cycle increment $\Delta N_{inc}|_s$. Finally, all elements for which:

$$\frac{\Delta N_{onset}|_k}{\Delta N_{inc}} < 1 + f \tag{20}$$

where $f = 0.1$, are considered to fail in step k.

Propagation Zone

Previously, VCCT was used to simulate crack growth from an assumed damage state [10]. This methodology assumes LEFM and hence, that stresses tend to infinity at the crack front. Consequently, these assumptions prevent use of an approach that predicts damage onset using a stress-based failure criterion, since refinement in the vicinity of the crack tip would lead to continuously increasing stress, rendering a mesh-subjective approach. For sufficient refinement (high stress at the crack tip), propagation of a crack would no longer be controlled by a fracture mechanics criterion, but always governed by the stress-based onset criterion. Therefore, a zone of length l_{th} must be defined, within which the onset criterion is not activated.

For further clarification, let us first assume predominantly Mode I loading. The stresses ahead of a crack tip can be estimated by:

$$\sigma(x) = \frac{K_I}{\sqrt{2\pi x}} + O(x) \tag{21}$$

where K_I is the Mode I stress intensity factor, and x the distance from the crack tip along the crack path (Figure 3). Assuming plane strain conditions and neglecting higher order terms, one can write:

$$\sigma(x) \approx \frac{\sqrt{G_I E}}{\sqrt{2\pi x}} \tag{22}$$

in which G_I is the Mode I energy release rate and E the Young's modulus.

In fatigue, it is generally possible to assume a threshold stress level, σ_{th}, below which fatigue onset is assumed not to occur within the number of cycles of interest. Using Equation 22, it is possible to determine a distance away from the crack tip, l_{th-I}, associated with Mode I loading, where the stresses caused by the presence of a crack decay below σ_{th}:

$$l_{th-I} \approx \frac{G_I E}{2\pi\sigma_{th-n}^2} \tag{23}$$

The same approximation can be made for Mode II loading. Additionally, if the critical energy release rates for Mode I and Mode II are assumed, G_{Ic} and G_{IIc}, a further conservative estimate can be obtained:

$$l_{th-Ic} \approx \frac{G_{Ic}E}{2\pi\sigma_{th-n}^2}, \ l_{th-IIc} \approx \frac{G_{IIc}E}{2\pi\sigma_{th-s}^2} \tag{24}$$

where the subscripts n and s designate shear and normal tractions. Finally, the maximum distance l_{th}, can be approximated by:

$$l_{th} = \max\{l_{th-Ic}, l_{th-IIc}\} \tag{25}$$

The distance l_{th} can then be used to define an area within which the onset criterion is not activated (Figure 3).
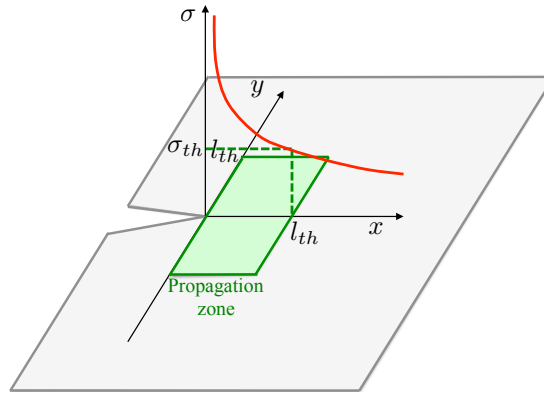

Figure 3. Definition of the propagation zone, within which the onset criterion is not activated.

VERIFICATION

The approach outlined above was implemented in Abaqus/Standard®. The user subroutine SDVINI was used to seed the elements with the initial strength values, obtained by randomly sampling a Weibull distribution. The extended interface element was implemented as a 3D UEL (user element subroutine). In addition, the user subroutine UEXTERNALDB was used to interface with an external Python script. This script is used to manage the crack insertion and propagation. To verify the approach, two sets of verification exercises were performed, the first dedicated to matrix cracks, and the second to delaminations.

Matrix Cracks

To assess the accuracy of the energy release rate calculation for matrix cracks, numerical results are compared to the analytical solutions for an orthotropic plate with a center crack under Mode I and Mode II loading conditions. The elastic properties are

assigned such that the fiber direction is aligned with the crack, in a similar fashion to what was performed in [11]. Two cases were considered, one corresponding to Mode I (Figure 4a), and another to Mode II (Figure 4b). The model is a square plate of 50×50 mm in-plane and 1 mm thickness. A crack of 5 mm length is assumed to be located at the center of the plate. The plate was loaded with applied tractions as illustrated in Figure 4. The center region of the specimen was progressively refined to assess the accuracy and mesh objectivity of the approach. Numerical results were compared to analytical solutions for Mode I [12]:

$$G_I = \frac{\sigma_\infty^2 \pi a}{\left[\dfrac{4G_{12}E_1 E_2^{3/2}}{2G_{12}E_1^{1/2} + E_1 E_2^{1/2} - 2\nu_{12}G_{12}E_2^{1/2}} \right]^{1/2}} \tag{26}$$

and Mode II [12]:

$$G_{II} = \frac{\tau_\infty^2 \pi a}{\left[\dfrac{4G_{12}E_1^2 E_2^{1/2}}{2G_{12}E_1^{1/2} + E_1 E_2^{1/2} - 2\nu_{12}G_{12}E_2^{1/2}} \right]^{1/2}} \tag{27}$$

energy release rates, where σ_∞ and τ_∞ are the normal and shear remote loadings and a is half of the crack length (Figure 4). The variables E, G and ν are the in-plane Young's modulus, shear modulus and Poisson ratio. The subscripts '1' and '2' refer to fiber direction and transverse direction, respectively.

Figure 4 shows that, for the same refinement, Mode II results have a slightly larger error than Mode I. Nevertheless, for both loading modes, the solution is demonstrated to converge to the analytical value.
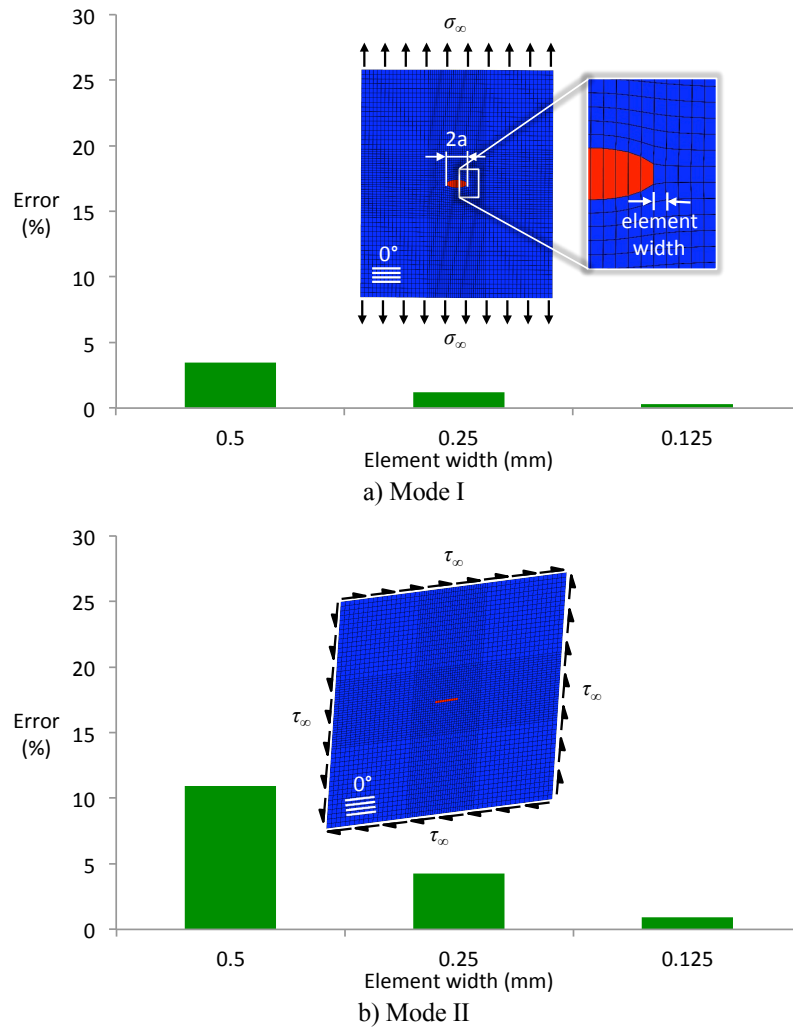
a) Mode I

b) Mode II

Figure 4. Energy release rate error between numerical and analytical solutions as a function of the mesh refinement.

Delaminations

In [13, 14], numerical benchmarks were proposed to assess the accuracy of fracture mechanics based approaches to simulate delamination propagation under Mode I and Mode II fatigue loading. The numerical models used correspond to Double Cantilever Beam (DCB) and End-Notch-Flexure (ENF) specimens. These benchmarks were used in the present work to assess the accuracy and correct implementation of the approach for delamination propagation. The mesh, material properties, and load conditions were prescribed following [13, 14] and for brevity are not repeated here. The results obtained are provided in Figure 5, where the maximum crack length at each step is plotted against number of cycles and compared to the benchmark results [13, 14]. Further mixed-mode cases showing similar acceptable agreement, and a detailed comparison to the current Abaqus/Standard® low-cycle fatigue capability, are provided in [15].
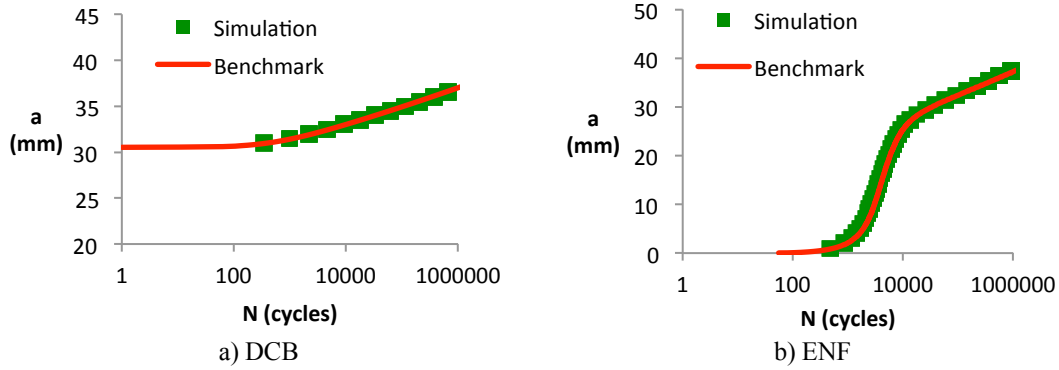
a) DCB   b) ENF

Figure 5. Comparison between the numerical results obtained for Mode I (DCB) and Mode II (ENF) loadings and the benchmarks provided in [13, 14].

APPLICATION

To demonstrate the adequacy of the approach to capture the onset and accumulation of multiple cracks, the experiment proposed in [16] was simulated. In [16], two different laminates with the same stiffness were considered. In laminate A, $[0_3, \mathbf{90}, 0_8, \mathbf{90}, 0_3]$, the two 90° plies are isolated, while in laminate B, $[0_7, \mathbf{90_2}, 0_7]$, they are stacked in the center of the specimen. Specimens with the same dimensions were manufactured from the two laminates. The specimens were loaded under uniaxial tension-tension fatigue at the same load level, σ_{max}, corresponding to 60% of the ultimate strength with a 0.1 load ratio and a frequency of 10 Hz. Experimental results showed that the damage accumulation in fatigue was markedly different for the two layups [16]. Specimens from laminate A exhibited a significantly higher crack saturation density than from laminate B. Contrarily, matrix cracks in laminate B grew faster and to a greater length than in laminate A. Additionally, the authors highlighted the importance of capturing the 3D effects caused by the interaction and shielding of cracks growing through the width. Indeed, two-dimensional (2D) analysis would assume cracks would traverse the specimens completely. However, this was seldom observed experimentally, with cracks arresting before traversing the specimen, due to the interaction with other growing cracks. In [16], the material used in the experiments was carbon/epoxy T300/914. In the present work, due to a lack of a complete set of fatigue material data for T300/914, properties for the carbon-epoxy IM7/8552, which has similar elastic properties (~15% difference in E_{11}), were assumed instead.

Material properties and input data

In this section, the material properties and input data used in the application example are summarized. The elastic properties assumed for IM7/8552 are provided in Table I.

TABLE I. ELASTIC PROPERTIES, IM7-8552 [17]

E_{11}	$E_{22} = E_{33}$	$\nu_{12} = \nu_{13}$	ν_{23}	$G_{12} = G_{13}$	G_{23}
161.0 (GPa)	11.38 (GPa)	0.32	0.44	5.17 (GPa)	3.98 (GPa)

In [10], S-N data for the transverse strength of IM7/8552 using 3PB and 4PB tests were produced. In the present work, the 3PB results were used, since they required the least amount of scaling. A least squares fit of an S-N curve, as given in equation 19, to the average of the failure strength obtained for each load level, yielded $\alpha = 0.071$ with a correlation coefficient of $R^2 = 0.95$. The Weibull characteristic strength, σ_c, and shape parameter, m, were also obtained from [10]. The material properties used to determine crack onset, together with the assumed threshold value, σ_{th}, are given in Table II. The same S-N curve is used to model both matrix crack (intra-laminar) and delamination (inter-laminar) onset. This assumption is a first approximation and can be updated as reliable experimental data are obtained. Nevertheless, the equivalence between intra-laminar and inter-laminar Mode I critical energy release rate has been experimentally demonstrated for IM7-8552 [18].

TABLE II. MATERIAL PROPERTIES USED TO PREDICT CRACK ONSET IN THE PRESENT STUDY

α	σ_c MPa [17]	m [17]	σ_{th} MPa
0.071	128.95	18.83	60.0

To model crack growth, the growth rate obtained in [19-21] for pure Mode I, Mode II and mixed-mode I/II is linearly interpolated to obtain the Paris Law coefficient and exponent, c and n, in equation 7. The values used are summarized in Table III.

TABLE III. PARIS LAW COEFFICIENT c AND EXPONENT n AS A FUNCTION OF THE MODE-MIXITY β. NORMALIZED DATA ARE CONSIDERED FOR ALL β EXCEPT $\beta = 1.0$

	$\beta = 0$	$\beta = 0.2$	$\beta = 0.5$	$\beta = 0.8$	$\beta = 1.0$
c	173.83	2291.31	6.90	4.29	0.231
n	6.77	8.38	5.41	5.07	5.45

Results

The models used are illustrated in Figure 6. For laminate A, symmetry conditions were applied, and only half of the thickness was considered (Figure 6a). For laminate B, no symmetry conditions were applied, due to the difficulty in adding boundary conditions as damage evolved (note that no pre-defined damage location is assumed) (Figure 6b). The two elements near the boundaries where traction is applied were not allowed to fail - 'no failure' zone. This prevented numerical issues and ensured regular load introduction throughout the analysis. In both cases, the lengthwise dimension was assumed to be 2.0 + 0.18 mm, where 0.18 is the length of the 'no failure' zone. The use of a representative region, rather than the full specimen, enables a significant reduction in the computational time. For laminate A, FNM elements were used in the center of the specimen. Each element modeled half of the ply above and below the 90/0 interfaces. For laminate B, one additional FNM element was used in the center region, modeling half of the ply above and below the mid-plane 90/90 interface. Elsewhere in the models, native Abaqus/Standard elements C3D8 (bi-linear, full integration) were used. Tensile fatigue loading, σ_{max}, was applied corresponding to approximately 60% of the ultimate strength, as in [16]. Assuming the 0° plies will carry the final failure load, σ_{max} was estimated to be:

$$\sigma_{max} = 0.6n_{0°}X_T \qquad (28)$$

where $X_T = 2560$ MPa is the fiber tensile strength of IM7/8552 [22], and $n_{0°}$ is the number of 0° plies in the laminates. Figure 6 also shows the damage state obtained after 5×10^6 cycles. Qualitatively, it is possible to see the marked differences in crack density observed at the edges in the two laminates. Laminate A shows a significantly higher crack density at the edges of the two specimens compared to B. This is in agreement with the experimental observations. Furthermore, in Figure 7, it is also clear that not only the crack density differs, but also the average crack length: Laminate B shows fewer longer cracks. Once again, this is in agreement with what was reported in [16]. Additionally, the crack shielding, also reported in [16], can be observed in both laminates. Figure 8 compares the crack density accumulation observed experimentally and obtained numerically. The numerical results show similar trends to the experimental observations. In a first stage, Laminate B shows higher crack density than A. The cross-over point coincides approximately with the saturation density for Laminate B. After this stage, laminate A continues to accumulate cycles until saturation is reached. Quantitatively, the simulations show an overall higher crack density than that obtained experimentally. Moreover, more cycles are needed to obtain saturation. Indeed, saturation was only obtained for laminate A after 5×10^6 cycles (squares with dark outline). However, it is interesting to observe that the difference in saturation density between laminates A and B, Δ_{cds}, is approximately the same in both experiments and simulations, despite the differences in absolute values of crack density. It is worth recalling that the material simulated is not the same material used in the experiments, which may contribute to the quantitative differences observed. Nevertheless, the qualitative agreement demonstrates that the approach is able to simulate both onset and growth of multiple cracks and has the potential to capture the complex fatigue damage development, being able to simulate the development of distinct damage patterns in two seemingly equivalent laminates.
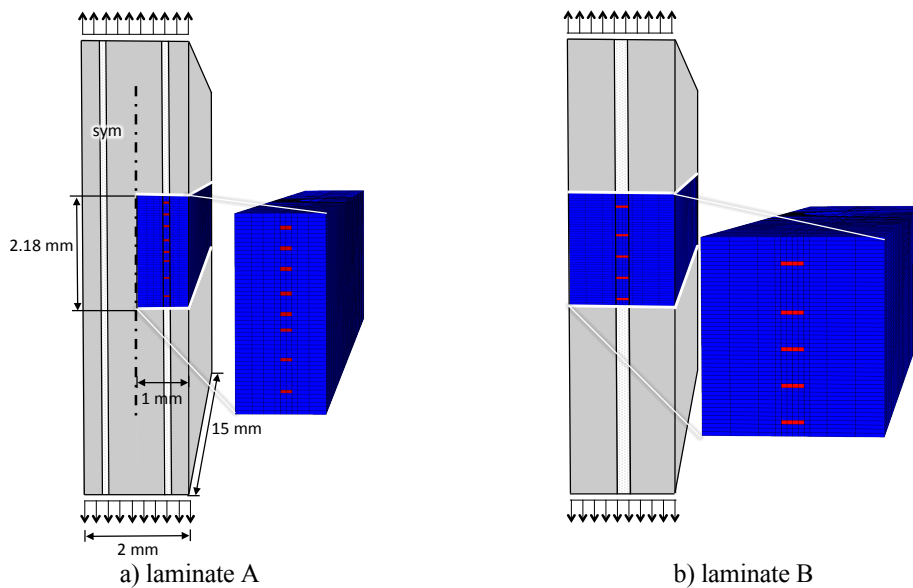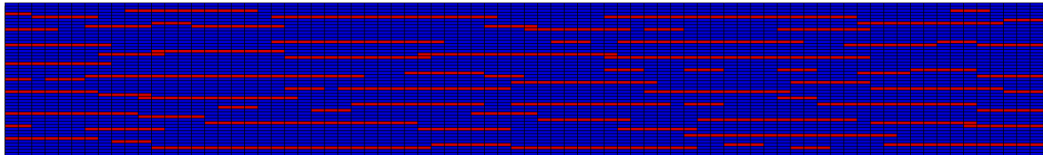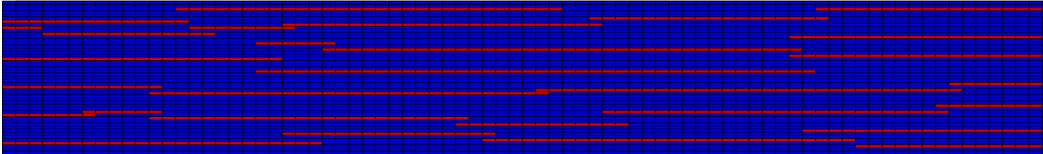

a) laminate A   b) laminate B

Figure 6. Numerical model dimensions and loading. Edge crack density after $N \approx 5\times10^6$ cycles. Laminate A shows a higher number of cracks at the edges (elements in red) compared to Laminate B.

a) laminate A

b) laminate B

Figure 7. Planar view of the 90 ply matrix cracks after $N \approx 5 \times 10^6$ cycles. Fewer longer cracks are observed in B compared to A. Crack shielding is evident in both specimens.
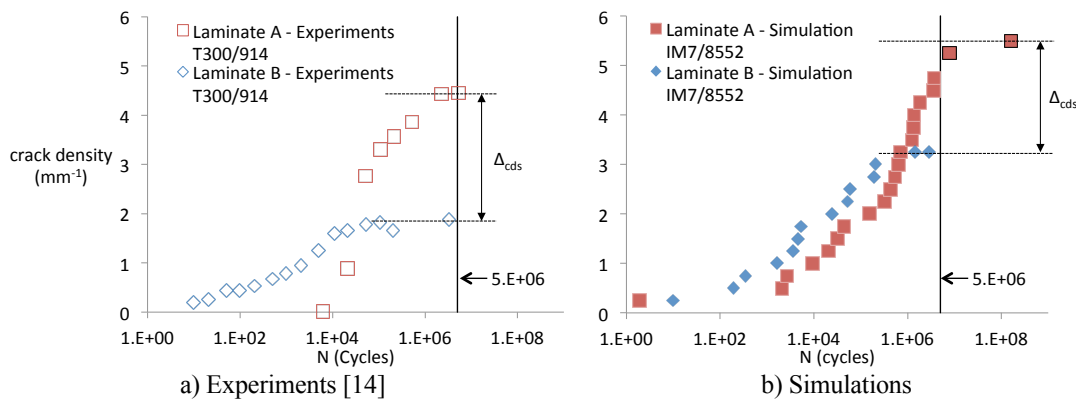

a) Experiments [14]

b) Simulations

Figure 8. Comparison between the observed and predicted crack density.

CONCLUSIONS

A new approach is proposed to model damage onset and accumulation in fatigue. It uses an extended interface element, based on the FNM method, to represent delaminations and matrix cracks. Crack propagation is determined using an element-based Virtual Crack Closure Technique and a Paris-Law relationship. Crack onset is determined using a stress-based onset criterion and Miner's rule to account for fatigue damage accumulation. The approach is implemented in Abaqus/Standard® via the user subroutine functionality. Preliminary verification shows good agreement between the numerical results obtained and analytical solution/benchmarks. Finally, the approach is demonstrated by capturing the experimentally observed differences in damage development and morphology between two seemingly equivalent cross-ply laminates, involving multiple crack onset and propagation.

REFERENCES

1. Fang, E., N. Simon, and J. Lua. 2014. "A Continuum Damage and Discrete Crack Module for Fatigue Damage Prediction of Laminated Composite Structures," presented at the 55th AIAA/ASME/ASCE/AHS/ASC Structures, Structural Dynamics, and Materials Conference, 13-17 January, 2014.

2. Hoos, K., E. V. Iarve, M. Braginsky, E. Zhou, and D. H. Mollenhauer. 2016. "Progressive Failure Simulation in Laminated Composites under Fatigue Loading by Using Discrete Damage Modeling," presented at the 57th AIAA/ASCE/AHS/ASC Structures, Structural Dynamics, and Materials Conference, 4-8 January, 2016.
3. Chen, B. Y., S. T Pinho, N. V. De Carvalho, P. M. Baiz, and T. E. Tay. 2014. "A Floating Node Method for the Modelling of Discontinuities in Composites," *Engineering Fracture Mechanics*, 27:104-134.
4. Rybicki, E. F., M. F. Kannine. 1977. "A Finite Element Calculation of Stress Intensity Factors by a Modified Crack Closure Integral," *Engineering Fracture Mechanics*, 9:931-938.
5. Paris, P. C., M. P. Gomez and W. E. Anderson. 1961. "A Rational Analytic Theory of Fatigue," *The Trend in Engineering 13, 9-14.*
6. Miner, M.A. 1945. "Cumulative Damage in Fatigue," *Journal of Applied Mechanics* 67:A159-A164.
7. May, M. and S. R. Hallett. 2011. "An Advanced Model for Initiation and Propagation of Damage Under Fatigue Loading – part I: Model formulation," *Composites Structures*, 93:2340-2349.
8. Weibull, W. 1939. "A Statistical Theory of the Strength of Materials," *Ing. Vetenskaps Akad. Handl.* (*Royal Swedish Institute Engineering Research Proceedings*), NR151, 1939.
9. O'Brien, T. K., A. D. Chawan, R. Krueger, and I. Paris. 2001. "Transverse Tension Fatigue Life Characterization Through Flexure Testing of Composite Materials," NASA/TM-2001-211035, 2001.
10. De Carvalho, N. V., B. Y. Chen, S. T. Pinho, J. G. Ratcliffe, P.M. Baiz, and T.E. Tay. 2015. "Modeling Delamination Migration in Cross-Ply Tape Laminates," *Composites Part A: Applied Science and Manufacturing*, 71:192-203.
11. Mabson, G. E., O. Weckner and M. Ramnath. 2012. "Finite Element Based Decohesive Failure Simulation Sensitivity Studies," presented at the 57th AIAA/ASCE/AHS/ASC Structures, Structural Dynamics, and Materials Conference, 23-26 April, 2012.
12. Sih, G. C., P. C. Paris, G. R. Irwin. 1965. "On Cracks in Rectilinearly Anisotropic Bodies," *International Journal of Fracture Mechanics*, 1:189.
13. Krueger, R. 2010. "Development of a Benchmark Example for Delamination Fatigue Growth Prediction," NASA/CR-2010-216723.
14. Krueger, R. 2011. "Development and Application of Benchmark Examples for Mode II Static Delamination Propagation and Fatigue Growth Predictions," NASA/CR-2011-217305.
15. Krueger, R. and N. V. De Carvalho. 2016. "In Search of a Time Efficient Approach to Crack and Delamination Growth Predictions in Composites," to be presented at the 31st ASC Technical Conference, 19-21 September, 2016.
16. Lafarie-Frenot, M. C. and C. Hénaff-Gardin. 1991. "Formation and Growth of 90° Ply Fatigue Cracks in Carbon/Epoxy Laminates," *Composites Science and Technology* 40:307-324.
17. O'Brien, T.K., R. Krueger. 2003. "Analysis of Flexure Tests for Transverse Tensile Strength Characterization of Unidirectional Composites," *Journal of Composites Technology and Research,* 25:50-68.
18. Czabaj, M. W. and J. G. Ratcliffe. 2013. "Comparison of Intralaminar and Interlaminar Mode I Fracture Toughnesses of a Unidirectional IM7/8552 carbon/epoxy composite," *Composites Science and Technology* 89:15-23.
19. Murri, G. B. 2013. "Evaluation of Delamination Onset and Growth Characterization Methods Under Mode I Fatigue Loading," NASA/TM-2013-0010557.
20. Ratcliffe, J. G. and W. M. Johnston. 2014. "Influence of Mixed Mode I-Mode II Loading on Fatigue Delamination Growth Characteristics of a Graphite," presented at the 29th ASC Technical Conference, 8-10 September, 2014.
21. O'Brien, T. K., W. M. Johnston, and G. J. Toland. 2010. "Mode II Interlaminar Fracture Toughness and Fatigue Characterization of a Graphite Epoxy Composite Material," NASA/TM-2010-216838.
22. Kaddour, A. S., M. J Hinton, P. A. Smith, and S. Li. 2013. "Mechanical Properties and Details of Composite Laminates for the Test Cases Used in the Third World-Wide Failure Exercise," *Journal of Composite Materials*, 47(20-21):2427-2442.